Journal of Applied Engineering Science & Technology Vol. 6 No. 2 (2026) 148

Issues lists available at UMKB journals

Journal of Applied Engineering Science & Technology

Journal home page: https://journals.univ-biskra.dz/index.php/jaest

https://doi.org/10.69717/jaest.v6.i2.148

Performance Analysis and Optimization of $BaHfS_3$-Based Solar Cells Using SCAPS-1D Simulation Software

Soko Swaray[1, *], Muteeu A. Olopade[1, 2]

[1]*Department of Physics, Fourah Bay College, University of Sierra Leone, Sierra Leone*
[2]*Department of Physics, University of Lagos, Nigeria*

ABSTRACT

Although early theoretical studies and experimental studies indicate the potential of Barium Hafnium Sulfide ($BaHfS_3$) as a photovoltaic absorber material, comprehensive device-level research under practical working conditions remains minimal. Chalcogenide $BaHfS_3$ is a lead-free absorber layer material that has garnered attention because of its promising optical absorption and potential stability for solar energy technology. In this research, $BaHfS_3$-based solar cell designs are investigated through Solar Cell Capacitance Simulator (SCAPS-1D) software numerical modeling. Optimization aspects of the device, such as absorber thickness, bandgap energy, defect density, operating temperature, parasitic resistances, buffer layer thickness, and charge transport material are considered. The base model ($AZO/IGZO/BaHfS_3/Sb_2S_3$) recorded an η of 8.78 %, FF of 52.67 %, Jsc of 19.90 mA/cm^2, and Voc of 0.837 V. The absorber thickness ranging from 300-400 nm presents a fair compromise between light absorption and carrier transport, Voc starts at 0.90 V and decreases to 0.84 V, Jsc rises from 23 mA/cm^2 to 27 mA/cm^2, FF declines from 75 % down to 30% and recorded and efficiency of 16.1 %, while bandgap energy tuning showed a maximum η of 16.2 % at 1.5 eV. Lowering absorber defect density to Nt = 1 × 10^{10} cm^{-3} enhances device performance, where Voc = 0.86 V, Jsc = 27 mA/cm², FF = 83 % and η increased to 19 %. Thermal effects were modest, with η of 18.8 % at the temperature between 340 and 350 K. Under optimized parasitic resistances, series resistance (Rs) recorded η of 18.7 % as Rs varies from 1–10 Ω·cm^2, whereas shunt related losses severely degraded η to 1.59 %. Increasing $MoSe_2$ layer thickness improved the η from 18.7 % to 25.39 % at the thickness of 1000 nm. In the transport layers studies Ti_2O_3 is identify as the most effective ETM and CuS as the best HTM. The optimized $TiO_2/BaHfS_3/CuS$ device achieved an efficiency of 19 % due to favorable Type-II band alignment and efficient charge separation. $BaHfS_3$ can be a promising absorber material for the next-generation photovoltaic applications, and these findings confirm its potential.

KEYWORDS

$BaHfS_3$
Solar cells
SCAPS-1D
Photovoltaic
Absorber

ARTICLE HISTORY	Received	Revised	Accepted	Published
	25 Dec 2025	17 Mar 2026	25 Avr 2026	11 Jul 2026

1 Introduction

Renewable energy is when natural resources like sunlight, tidal, biogas, wind, and hydropower are continuously replenished for generating electricity in a sustainable manner [1]. Of these resources, renewable energies such as solar energy can be particularly attractive due to accessibility and abundant availability [2]. Photovoltaic cells absorb radiant energy and transform it into electrical energy via the photovoltaic effect. As such, such clean energy technology becomes vital for minimizing reliance on CO_2 energy sources, reducing methane (CH_4) and nitrous oxide (N_2O) emissions, and promoting a sustainable power future [3]. They are increasingly important

for solving global energy problems, offering clean, reliable, and scalable alternatives to fossil fuels [4]. Besides its environmental advantages, it improves energy security, decentralizes power production, and also generates economic development through job creation in installation, manufacturing, and maintenance industries [5]. With increasing demand for sustainable solutions, solar cells form the basis of a resilient and carbon-neutral energy future that is crucial. $BaHfS_3$ is an orthorhombic chalcogenide perovskite that has recently been identified as a promising lead-free material owing to its advantageous light absorption properties and potential stability [6]. The fundamental bandgap of this material has been estimated in various ways. First-principles DFT calculations (Materials Project) suggest a direct bandgap of approximately 1.24 eV for the ground state crystal structure. In terms of quantity or quality, based on sample quality and composition, band gap measurements as high as ~2.06-2.0 eV (in bulk or powder) has been reported experimentally with UV diffuse reflectance and Tauc plot studies. For example, powdered $BaHfS_3$ is reported as having an optical band gap close to 2.06 eV [7]. Studies on alloying with Zr in ($BaHfS_{3-x}Zr_xS_3$) have been conducted synthetically and through SCAPS-1D device simulations, which showed that the lattice parameters and band gap show a linear effect with the composition [8]. This shows that selective alloying can tilt the absorption edge towards the visible spectrum, which could increase the

* Corresponding author. Soko Swaray *(S. Swaray)*
E-mail : sokoswaray264@gmail.com

theoretical power conversion efficiencies (PCEs) to more than 20 % under optimal conditions [9]. By incorporating Zr into $BaHfS_3$, the performance of solar cells was enhanced, as demonstrated through the analysis of chalcogenide perovskite cells using SCAPS-1D, which included $BaHfS_3$, $BaHf_{0.75}Zr_{0.25}S_3$, and $BaHf_{0.25}Zr_{0.75}$. The solar cells with the FTO/TiO_2/BaHf1-xZrxS_3/NiO/Au configuration achieved power conversion efficiencies of 14.26 %, 16.75 %, 19.28 %, and 21.94 % [10]. This improvement is attributed to the increased built-in potential (~1.5 V), longer diffusion length (~0.4), higher absorption rate (51.05 %), and greater recombination resistance. A DFT study of $BaHfS_3$ under varying pressure conditions revealed a photovoltaic efficiency of 28.68 % with a band gap of 1.30 eV in the visible spectrum [11]. First-principles calculations indicated that orthorhombic $BaHfS_3$ is both energetically and mechanically stable, exhibiting a ductile nature. The material demonstrates strong absorption (~105 cm^{-1}) and low reflectivity (< 40 %) in the visible range, making it a promising candidate for solar-cell absorbers and photocatalysts. The simulation of the $BaHfS_3$-based solar cell structure reached a peak power conversion efficiency of 23.65 % at a thickness of 900 nm [12]. Notwithstanding these promising theoretical and preliminary experimental outcomes, until now, few works on full solar cells with $BaHfS_3$ absorbers that have resulted in high power conversion efficiencies under ambient conditions by means of SCAPS–1D are reported [13]. Additional studies are needed in thin film enhancement, defect correction, carrier lifetime management, interface engineering, and device design. This study aims to close this gap by utilizing SCAPS-1D numerical computer-based simulation to enhance the PCE of $BaHfS_3$ device through the optimization of various operational parameters under different conditions.

2 Methodology

2.1 Proposed Structure and Computational details

Figure 1 illustrates the configuration of the proposed $BaHfS_3$ solar cell with uniform material properties assumed in each layer. The $BaHfS_3$ solar cell was simulated using the solar cell capacitance simulator (SCAPS-1D) under the sunlight of AM1.5 G, 100 MW/cm^2 at a temperature of 300 K, metal work function of 5.2 Ev, absorption coefficient of 10^5 1/cm and a frequency of 1× 10^6 Hz. The top layer, composed of aluminum-doped zinc oxide (AZO), serves as a light-transmitting conductor for the collection of electrons. Meanwhile, the n-type indium gallium zinc oxide (IGZO) layer functions as the electron transport layer, which helps to minimize recombination losses. A molybdenum disulfide ($MoSe_2$) buffer layer enhances band alignment between the electron transport layer and the absorber. Charge carrier generation occurs within the p-type $BaHfS_3$ absorber layer, whose thickness lies in the 100 – 1000 nm range. Additionally, the tin sulfide (SnS) layer forms a back-surface field that further reduces recombination events, while the antimony sulfide (Sb_2S_3) layer aids in hole transport. Equations 1-5 detail aspects such as potential distribution, carrier transport, recombination process, and band alignment [14, 15], supported by the input numerical data in Table 1-3.

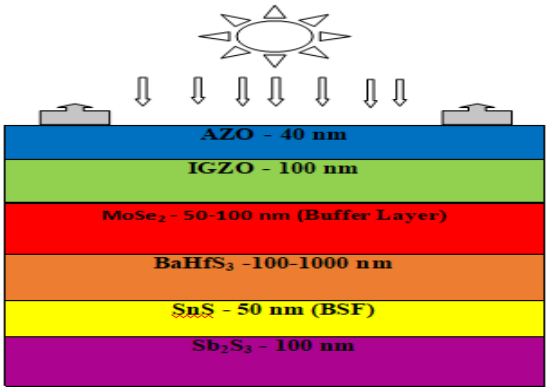

Fig. 1. Schematic Structure of the Proposed $BaHfS_3$-Based Thin-Film Solar Cel.

$$\nabla^2\phi = \frac{\rho}{\varepsilon} \quad (1)$$

$\boldsymbol{\phi}$ is the electrostatic potential, **ρ** is the charge current density, and **ε** is the permittivity of the material.

$$\frac{\partial n}{\partial t} = \frac{1}{q}\nabla . J_n + G - R \quad (2)$$

$$\frac{\partial p}{\partial t} = -\frac{1}{q}\nabla . J_p + G - R \quad (3)$$

n and **p** are electron and hole concentrations, $\boldsymbol{J_n}$ and $\boldsymbol{J_p}$ are current densities, **G** is the generation rate, and **R** is the recombination rate.

$$\Delta E_c = X_{ETL} - X_{Abs} \quad (4)$$

$$\Delta E_v = \left(E_g^{Abs} - E_g^{ETL}\right) - \Delta E_c \quad (5)$$

$\boldsymbol{\Delta E}$c and $\boldsymbol{\Delta E}$v are conduction and valence band offsets.

Table 1. Computational input parameters used in the simulation process.

Parameters	Sb_2S_3 [16]	SnS [17]	$BaHfS_3$ [10]	$MoSe_2$ [18]	IGZO [19]	AZO [20]
Thickness (nm)	100	50	100 - 1000	50 -1000	100	40
Bandgap (eV)	1.62	1.31	1.7	1.29	1.51	3.3
Electron affinity (eV)	3.7	4.3	4.1	4.2	4.16	4.52
Dielectric permittivity	7.08	13	9.6	9	10	9
CB (cm^{-3})	2.2×10^{19}	1.8×10^{18}	2.2×10^{18}	7.0×10^{17}	5.0×10^{18}	1.8×10^{19}
VB (cm^{-3})	1.0×10^{19}	4.7×10^{18}	1.0×10^{19}	1.8×10^{18}	5.0×10^{18}	2.2×10^{18}
Electron thermal velocity ($cm.s^{-1}$)	1.0×10^{7}	1.0×10^{7}	1.0×10^{7}	1.0×10^{7}	1.0×10^{7}	1.0×10^{7}
Hole thermal velocity ($cm.s^{-1}$)	1.0×10^{7}	1.0×10^{7}	1.0×10^{7}	1.0×10^{7}	1.0×10^{7}	1.0×10^{7}
Electron mobility (cm^2/VJ)	9.8	130	0.017	100	15	100
Hole mobility (cm^2/Vs)	10	50	0.059	150	10	25
ND (cm^{-3})	0	0	1.0×10^{10}	1.0×10^{9}	1.0×10^{15}	1.0×10^{19}
NA (cm^{-3})	1.0×10^{12}	1.0×10^{15}	1.0×10^{10}	1.0×10^{10}	1.0×10^{15}	1.0×10^{3}
Nt type	Donor	Neutral	-	Neutral	Acceptor	Neutral
Nt (cm^{-3})	1.0×10^{14}	1.0×10^{14}	1.0×10^{15}	1.0×10^{14}	1.0×10^{14}	1.0×10^{14}

Table 2. Compilation of various Hole Transport Materials (HTM) layers applied in the device simulation.

Parameters	CdSe [21]	Cu_2Te [22]	$BaSi_2$ [23]	CuS [24]	Cu_2O [25]	CuSCN [26]	MoS_2 [27]	MoO_3 [28]
Thickness (nm)	100	100	100	100	100	100	100	100
Bandgap (eV)	1.7	1.19	1.3	1.55	2.17	3.4	1.7	3
Electron affinity (eV)	3.93	4.1	3.3	3.6	3.2	1.9	4.2	2.5
Dielectric permittivity	9.5	10	11.170	6.5	7.11	7.08	13.6	12.5
CB (cm^{-3})	2.8×10^{19}	7.8×10^{17}	2.6×10^{19}	1.2×10^{19}	2.02×10^{17}	2.2×10^{18}	2.2×10^{18}	2.2×10^{18}
VB (cm^{-3})	1.2×10^{19}	1.8×10^{19}	2.0×10^{19}	1.8×10^{19}	1.0×10^{19}	1.8×10^{18}	1.8×10^{19}	1.8×10^{19}
Electron thermal velocity ($cm.s^{-1}$)	1.0×10^{7}	1.0×10^{7}	1.0×10^{7}	1.0×10^{7}	1.0×10^{7}	1.0×10^{7}	1.0×10^{7}	1.0×10^{7}
Hole thermal velocity ($cm.s^{-1}$)	1.0×10^{7}	1.0×10^{7}	1.0×10^{7}	1.0×10^{7}	1.0×10^{7}	1.0×10^{7}	1.0×10^{7}	1.0×10^{7}
Electron mobility (cm^2/VJ)	5.93	500	820	12	9.8	200	100	100
Hole mobility (cm^2/Vs)	25	100	100	9	10	80	25	25
ND (cm^{-3})	0	0	0	0	0	0	0	0
NA (cm^{-3})	1.0×10^{19}	1.0×10^{19}	1.0×10^{19}	1.0×10^{19}	1.0×10^{18}	1.0×10^{20}	1.0×10^{16}	1.0×10^{15}
Nt (cm^{-3})	1.0×10^{14}	1.0×10^{14}	1.0×10^{14}	1.0×10^{14}	1.0×10^{14}	1.0×10^{14}	1.0×10^{14}	1.0×10^{14}

Table 3. Compilation of various Electron Transport Materials (ETM) layers applied in the device simulation.

Parameters	Ti_2O_3 [29]	ZnO [30]	WS_2 [31]	Alq_3 [32]	$ZnSnN_2$ [33]	In_2S_3 [34]	C_6O [34]	ZnMgO [35]
Thickness (nm)	100	100	100	100	100	100	100	100
Bandgap (eV)	1.2	3.3	1.87	2.8	1.5	2.8	1.7	3.3
Electron affinity (eV)	4	4.6	4.3	4.17	4.1	4.6	3.9	3.9
Dielectric permittivity	8.9	9	11.9	3.4	15	13.5	4.2	12.5
CB (cm^{-3})	5.2×10^{18}	2.2×10^{18}	2.4×10^{19}	1.44×10^{20}	1.2×10^{18}	2.2×10^{17}	1.2×10^{18}	2.2×10^{18}
VB (cm^{-3})	1.8×10^{18}	1.8×10^{19}	1.0×10^{19}	1.44×10^{20}	7.8×10^{19}	1.8×10^{19}	7.8×10^{19}	1.8×10^{19}
Electron thermal velocity ($cm.s^{-1}$)	1.0×10^{7}	1.0×10^{7}	1.0×10^{7}	1.0×10^{7}	1.0×10^{7}	1.0×10^{7}	1.0×10^{7}	1.0×10^{7}
Hole thermal velocity ($cm.s^{-1}$)	1.0×10^{7}	1.0×10^{7}	1.0×10^{7}	1.0×10^{7}	1.0×10^{7}	1.0×10^{7}	1.0×10^{7}	1.0×10^{7}
Electron mobility (cm2/VJ)	10	100	260	0.0019	126	50	0.028	5
Hole mobility (cm^2/Vs)	10	25	51	0.0027	5.26	20	0.035	1
ND (cm^{-3})	1.0×10^{18}	1.0×10^{20}	0	1.0×10^{21}	0	0	2.6×10^{17}	1.0×10^{18}
NA (cm^{-3})	0	1.0×10^{15}	1.0×10^{16}	0	9.47×10^{19}	1.0×10^{17}	0	0
Nt (cm^{-3})	1.0×10^{14}	1.0×10^{14}	1.0×10^{14}	1.0×10^{14}	1.0×10^{14}	1.0×10^{14}	1.0×10^{14}	1.0×10^{14}

3 Results and discussions

Performance parameters of solar cells are determined by a number of material properties related to the ETM, such as its band gap, the position of the bottom of the conduction band with respect to the absorber material, the mobility of the charge carriers, and interfacial passivation. CuS and Ti_2O_3 were identified as the most efficient hole transport layer (HTLs) and electron transport layer (ETLs), respectively, for enhancing the efficiency of the $BaHfS_3$ solar cell. Ti_2O_3 works as the electron transport layer with a bandgap of 1.2 eV, which makes it always stay transparent and facilitates electron transport [36]. Its highly diluted valence level restrains hole diffusion, hence lowering recombination rates [37]. On the other hand, CuS serves as the hole transport layer, with appropriate work function for efficient hole collection. The $BaHfS_3$ absorbs charges efficiently owing to its band gap of 1.4-1.6 eV [38], which acts as a non-toxic alternative for lead halide perovskites [39]. The heterojunction of Ti_2O_3, $BaHfS_3$, and CuS yields Type-II band alignment, which promotes charge separation and avoids recombination loss. This kind of heterojunction has yielded remarkably high efficiency of 19% due to its successful absorption and separation of charges.

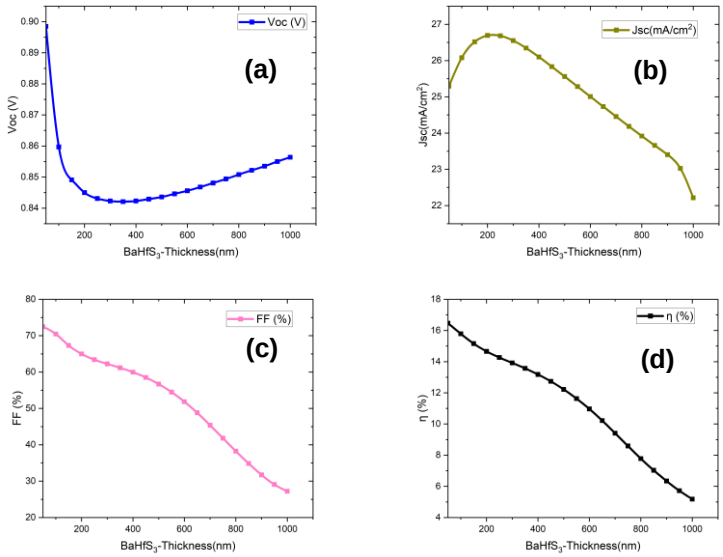

Fig. 2a-d. $BaHfS_3$ layer thickness effects on the photovoltaic parameters.

3.1 Modulating device performance by adjusting $BaHfS_3$ absorber layer thicknesses to optimize device efficiency

The absorber layer is the heart of a solar cell, which plays an important role by influencing light absorption, collection of charge carriers, and overall device efficiency [40]. Thin layers tend to capture fewer photons, resulting in a reduced photocurrent even when carrier collection is efficient [41]. Conversely, thicker layers can absorb more photons; however, this leads to increased recombination losses of charge carriers traveling longer distances, which becomes particularly challenging for materials with low mobility [42]. Figure 2a-d illustrates how the width of $BaHfS_3$ layer affects various photovoltaic metrics. The Voc starts at 0.90 V for thin layers, decreases to 0.84 V at a thickness of 200 nm, and increases again to 0.86 V at 1000 nm. This trend reflects a balance between free charge carrier losses and the influence of the force acting on a small positive charge [43]. The Jsc rises from 23 mA/cm^2 to 27 mA/cm^2 between thicknesses of 300-400 nm before dropping back to 23 mA/cm^2 at 1000 nm. The FF declines from 75 % down to 30 % at the maximum thickness due to heightened resistance losses. Optimal performance is observed with absorber layers ranging from 300-400nm thickness, yielding values of Voc at 0.85 V, Jsc at 27 mA/cm^2, FF at approximately 65%, and an efficiency of 16.1%. These results explain the process of how material takes in energy waves [44].

3.2 Influence of Band Gap Energy on the $BaHfS_3$ device

The Energy bandgap of an absorber material is a crucial parameter that influences the efficiency of solar cells [16]. It indicates the minimum energy at which the transition of an electron from the valence band to the conduction band takes place, thus creating electron-hole pairs, which are responsible for photocurrent generation. This parameter dictates not only the spectral response but also voltage and overall efficiency,

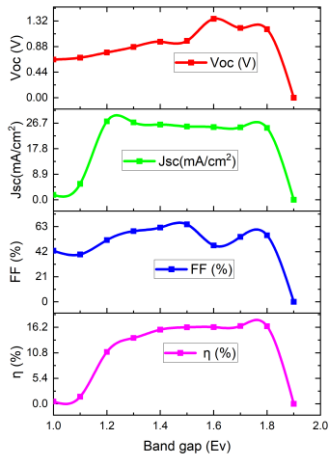

Fig. 3. Band Gap Energy on the Performance Parameters of $BaHfS_3$ Solar Cell.

which becomes vital during the construction of a high-performance photovoltaic device [45]. Figure 3 illustrates the impact of bandgap energy on the photovoltaic efficiency of $BaHfS_3$ solar cells. In the case of narrow bandgaps ranging from 1.0 -1.1 eV, enhanced photon absorption results in Jsc between 25 and 27 mA/cm^2, however, this is counterbalanced by a lower Voc of 0.45 V – 0.6 V, which constrains overall efficiency. The optimal performance occurs within the bandgap range of 1.4 -1.6 eV, where there is an ideal balance between photon absorption and carrier separation, resulting in Jsc values sustained at approximately 26-27 mA/cm^2 and Voc values rising to about 1.2-1.3 V. The fill factor remains stable around 45-46 %, culminating in a maximum efficiency of 16 %, aligning with Shockley-Queasier predictions of optimal devices at a bandgap of 1.4 eV. As

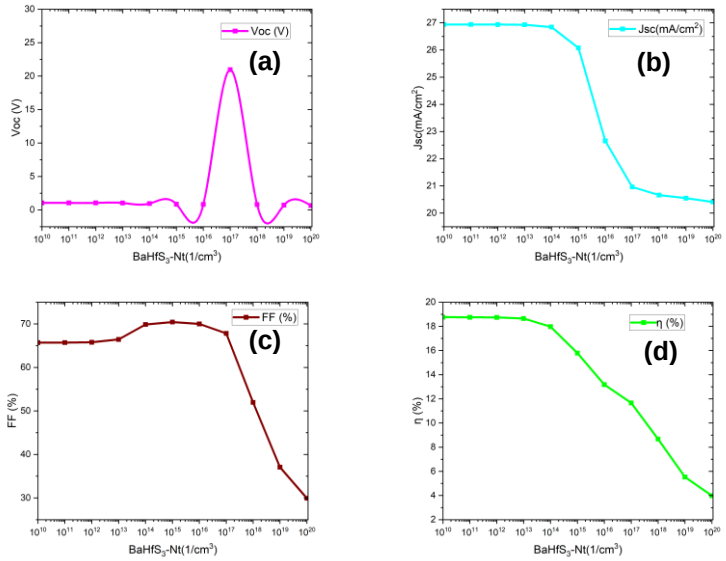

Fig. 4a-d. $BaHfS_3$ Absorber Defect Density on the Device Performance.

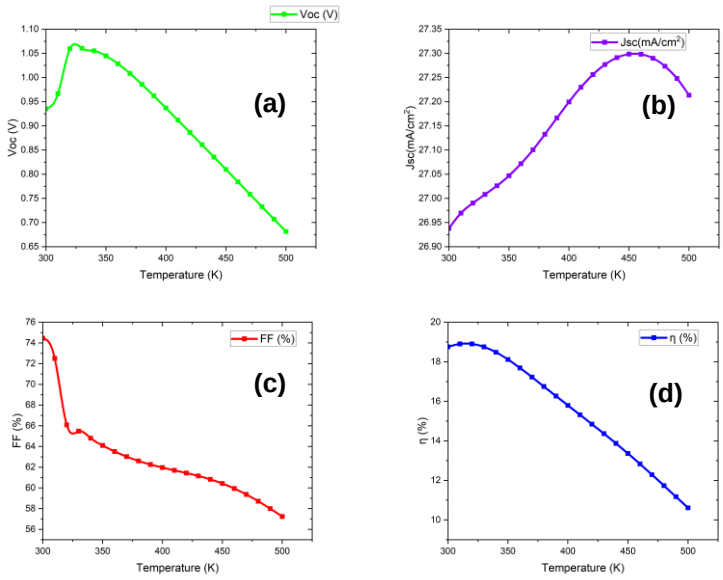

Fig. 5a-d. Impact of operational temperature on device performance.

the bandgap exceeds 1.6 eV, there is an observable degradation in efficiency due to a decrease in photon interactions across the bandgap that leads to fewer charge carriers and diminished Jsc values. Beyond a threshold of 1.8 eV, both photocurrent and Voc see significant reductions alongside decreasing fill factor. Data show a key trade-off between efficient photon absorption at lower bandgaps with higher voltage capacities at elevated gaps [46]. In the end, $BaHfS_3$ attains its peak efficiency of 16.2 % at a bandgap energy of 1.5 eV, optimizing absorption while minimizing recombination losses.

3.3 The role of Absorber defect density on the $BaHfS_3$ device

Adjusting the defect density in absorbers facilitates an investigation into how these imperfections influence carrier dynamics and overall efficiency, thereby informing the advancement of materials and device technologies [16]. This research optimized the absorber defect density from 1×10^{10} cm^{-3} to 1×10^{20} cm^{-3}. A reduction in defect density is associated with extended carrier lifetimes and improved conversion efficiency, while an excess of defects detrimentally impacts device performance Specifically, the open-circuit voltage (Voc) declined from 0.86 V to 0.21 V as the defect density increased from 1×10^{14} cm^{-3} to 1×10^{18} cm^{-3}, attributed to a rise in non-radiative recombination centers that decrease carrier lifetimes [47]. Similarly, the short-circuit current density (Jsc) decreases from 27 mA/cm^2 to 20.5 mA/cm^2 with higher Nt values of 1×10^{20} cm^{-3} due to recombination losses that hinder charge carrier collection [48]. The fill factor (FF) was also reduced from 70 % to 30 % at a defect density of 1×10^{20} cm^{-3} due to increased series resistance in the cell and reduced shunt resistance [49]. The relative overall efficiency (η) was considerably increased from the attain peak efficiency of 16.2% at a bandgap energy alignment to 19 % at minima defect density of 1×10^{10} cm^{-3} before decreasing 3% as the value of Nt increased to or beyond 1×10^{18} cm^{-3}, emphasizing the collective impacts of the values of Voc, Jsc, and FF. The impacts of the variables under study are well established and focus on the need for a low defect density in the absorber layer for efficient photovoltaic properties in $BaHfS_3$ solar cells, as illustrated in Figures 4a-d.

3.4 Thermal Effects on $BaHfS_3$ performance

The control of temperature is very important to keep the temperature stability of the BaHfS3 device [50]. The effect of temperature on the efficiency of photovoltaic cells

can be understood from Figure 5a–d. The open-circuit voltage (Voc) of the $BaHfS_3$ solar cells relates to temperatures non-linearly. The open circuit voltage (Voc) exhibits only a slight variation with temperature, increasing marginally from 0.94 V at 300 K to reach 1.05 V at 340 K. This weak dependence suggests that thermal effects on Voc are minimal within the investigated range. The short-circuit current density (Jsc) shows a very small increase from 26.94 mA/cm^2 at 300K to 27.30 mA/cm^2 at 450 K, which can be attributed to slight bandgap narrowing and strong optical absorption at elevated temperatures [25]. However, this change remains negligible. Although higher temperature can increase intrinsic carrier concentration and influence recombination mechanisms, the overall impact of Voc and Jsc is limited in this device [51]. Also, fill factor decreases from 74.1% down to 57 % while the temperature raises carrier concentration levels. It is due to the improvement in series resistance and reduction in shunt resistance. The maximum power conversion efficiency is 18.8 % in the range of 340-350 K, which evidences that at moderate heating, the better transport of carriers takes place and at extreme temperatures, it impairs the cell performance.

3.5 Effect of Series Resistance on $BaHfS_3$ Device Performance

Considering the reference efficiency of 18.8% obtained under the optimized temperature, we further optimize the influence of series resistance (Rs) on the BaHfS3 solar cell for an improve electrical properties and the result is depicted in Figure 6. As Rs changes from 1 Ω·cm^2 to 10 Ω·cm^2, the open-circuit voltage (Voc) remains steady at 1.08V, primarily governed by recombination mechanisms and the bult-in junction potential [52]. The short-circuit current density (Jsc) exhibits minimal fluctuation at 26.9 mA/cm^2, suggesting that carrier generation and collection are unaffected by variation in Rs. The fill factor (FF) experiences a slight increase from 74.5 % to 74.8 % as Rs increases, indicating minor internal resistive losses. The power conversion efficiency (η) remains nearly constant, with a slight decrease to 18.7 %. This minimal reduction suggests that the device performance is largely insensitive to the range of Rs examined, with sufficiently low internal resistive losses maintaining high photovoltaic performance [53].

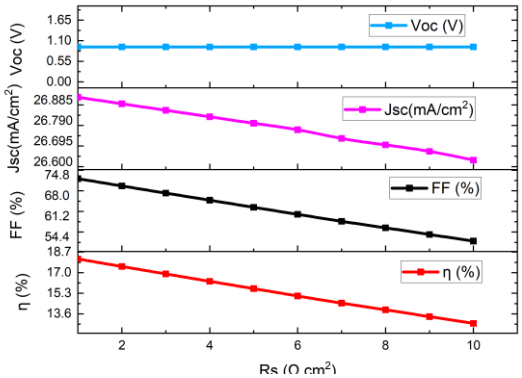

Fig. 6. Effect of Series Resistance on the Cell Performance.

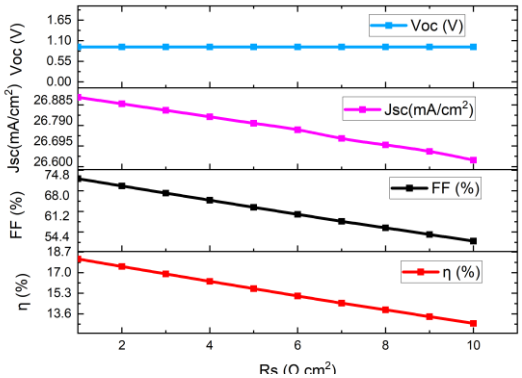

Fig. 7. Effect of Shunt Resistance on the cell Performance.

3.6 Effect of Shunt Resistance on $BaHfS_3$ Device Performance

Shunt resistance allows current to bypass the p-n junction across solar cell critically affecting efficiency and performance. The influence of shunt resistance (Rsh) on BaHfS3 photovoltaic device performance is illustrated in Figure 7. As Rsh varies from 1 Ω·cm^2 to 10 Ω·cm^2 the open-circuit voltage (Voc) decreases to 0.237 V, indicating a leakage current through parasitic pathways. The short-circuit current density (Jsc) remains nearly constant at 27 Ma/cm^2, while the fill factor (FF) exhibits minimal variation, ranging from 24.998 % to 25.02 %. Despite enhancements in Voc and FF, the power conversion efficiency remains below the optimal 18.8 %, decreasing to 1.59 % as Rsh vary from 1 Ω·cm^2 to Rsh = 10 Ω·cm^2. This reduction in efficiency signifies significant shunt-related losses, which create alternative current path that bypass the p-n junction [54]. Although increasing Rsh improves Voc and FF, the overall efficiency remains substantially below the baseline, underscoring the importance of minimizing shunt leakage pathways.

3.7 Effect of $MoSe_2$ Buffer Material Width on the $BaHfS_3$ Solar Cell

The buffer layer in solar cell is a semiconductor material placed between the absorber and window layers. In our research this layer plays a crucial role in enhancing efficiency by optimizing band alignment, reducing recombination, and improving the collection of charge carriers. Additionally, it stabilizes the interface, function as an optical window, and prevents undesirable chemical reaction. Therefore, the thickness of the buffer layer in solar cells plays a critical role in determining the interface, band gap, and charge transport between the absorber and window layers [55]. The optimal thickness is required for complete surface coverage, the least number of defects, and efficient charge separation along with light transmission [56]. For $MoSe_2$/$BaHfS_3$ heterojunctions, the optimal buffer thickness for $MoSe_2$ ranged from 100 to 1000 nm, contingent on specific passivation and band-offset criteria. The open-circuit voltage (Voc) rose from 0.940 V at a thickness of 100 nm to 0.950 V at 1000 nm due to the thicker $MoSe_2$ layer, which improved interface quality, decreased recombination rates, and augmented the built-in electric field. The short-circuit current density (Jsc) demonstrated fluctuations around 35.7 mA/cm^2 as a result of optical interference effects that alternately enhanced and diminishedlight absorption through constructive and destructive interference [57]. The fill factor (FF) increased to 75.18 % within the thickness range of 500-600 nm before fluctuating between 75.17 % to 75.18 % beyond 600 nm due to initially reduced recombination followed by increased series resistance. After incorporating $MoSe_2$ buffer layer and varying it thickness the power conversion efficiency (η) gradually increases from 18.7 % to 25.39 % at a thickness of 1000 nm, corresponding with an increase in Voc alongside stable light absorption levels. Although variations in FF and Jsc were observed, overall efficiency improved due to enhanced interface quality and lower recombination rates. Figures 8a-d show $MoSe_2$ acting as an optical and electrical buffer simultaneously for better quality of the junction with efficient light absorption.

3.8 Effect of the Hole Transport Materials on the $BaHfS_3$ Solar Cell

Figures 9a-d illustrate the role of hole transport material (HTM) selection on open-circuit voltage (Voc), fill factor (FF), and power conversion efficiency (η), while exhibiting minimal impact on short-circuit current density (Jsc). The open-circuit voltage is primarily dictated by the difference in quasi-Fermi levels when illuminated [58] . For an HTM to be effective, its valence band maximum must be positioned below that of the absorber layer [59]. Among the materials tested, CuS achieved the highest Voc at 0.871 V, whereas MoS_2 recorded the lowest at 0.3523 V. Jsc remained stable within a range of 29–30 mA cm^{-2} across all HTMs, as photon absorption is contingent upon the properties of the absorber. The role of HTM is more significant in influencing recombination and charge extraction than in generating photocarriers. The fill factor serves as an indicator of charge extraction efficiency and associated losses. High FF values were observed for CuS (72.01 %) and Cu_2Te (70.52 %), while MoS_2 demonstrated considerable losses with a FF of only 26.18%. In terms of power conversion efficiency, CuS outperformed with an efficiency of 16.56 %, compared to MoS_2 low value of 2.12 %. Energy band alignment plays a crucial role in facilitating hole transport. Both Cu_2O and Cu_2Te support hole mobility while inhibiting electron flow. Conversely, trap states present in MoS_2 detract from its performance. Doping is indeed necessary to optimize HTM performance by adjusting work functions, and it seems CuS is the best choice by far due to favorable band alignment. Table 4 present the results obtained from varying the selected hole transport materials.

3.9 Effect of the Electron Transport Materials on the $BaHfS_3$ Solar Cell

This study explores and analyses the effectiveness of various Electron Transport Materials (ETMs), such as Ti_2O_3, ZnO, WS_2, Alq_3, $ZnSnN_2$, In_2S_3, and ZnMgO as illustrated in Figures 10a-d and the results are recorded in Table 5 The evaluation focuses on critical photovoltaic performance metrics, including the open-circuit voltage (Voc), short-circuit current density (Jcs), fill factor (FF) and power conversion efficiency (PCE). ETMs are responsible for transporting electrons while not facilitating hole transfer, thereby

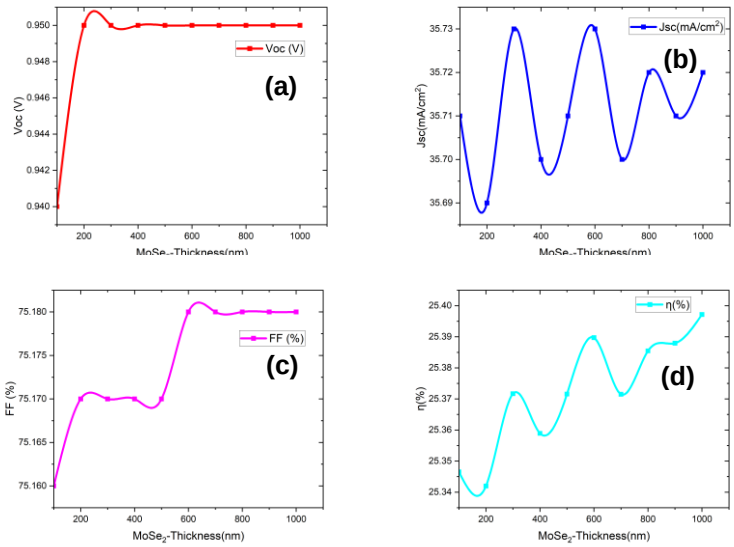

Fig. 8a-d. Effect of Buffer Layer Thickness on Solar Cell Performance.

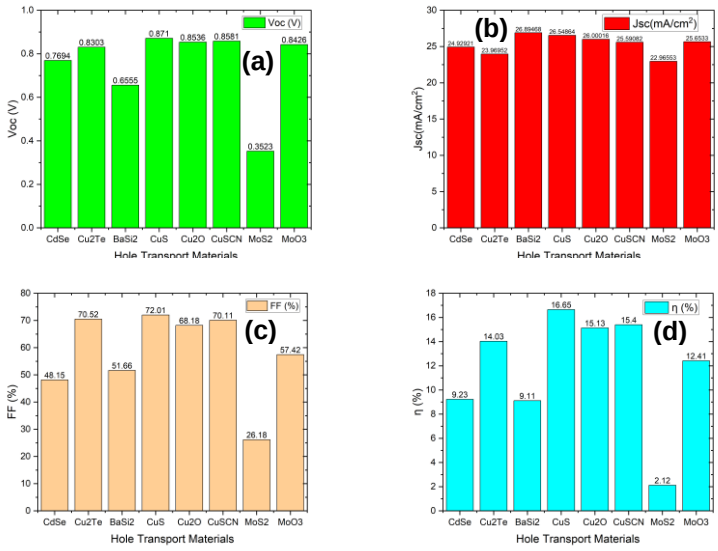

Fig. 9a-d. Evaluation of Hole Transport Materials in Solar Cells.

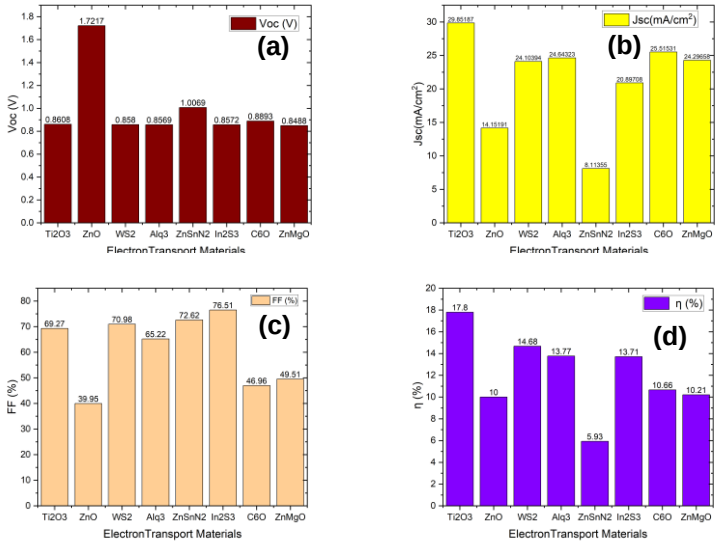

Fig. 10a-d. Evaluation of Electron Transport Materials in Solar Cells. Conclusion.

mitigating recombination losses [60]. Performance parameters of solar cells are determined by a number of material properties related to the ETM, such as its band gap, the position of the bottom of the conduction band with respect to the absorber material, the mobility of the charge carriers, and interfacial passivation [61]. Among the materials studied, ZnO achieves the highest Voc at approximately 3.73 V, followed closely by $ZnSnN_2$ with a Voc of about 3.15 V; other ETMs present lower Voc values ranging from around 0.84 to 0.88 V. Ti_2O_3 and C_6O demonstrate superior Jsc values at approximately 29.85 mA/cm² and 21.52 mA/cm² respectively due to their favorable electron mobility, whereas $ZnSnN_2$ shows a significantly lower Jsc at roughly 7.03 mA//cm_2. Ti_2O_3 is identify as the most effective ETM (Voc ≈ 0.8608 V, Jsc ≈ 29.85 mA/cm_2, FF ≈ 69.27 %, η ≈ 17.80 %).

Table 4. Results obtained from the optimization of different Hole Transport Materials (HTM).

HTL MATERIALS	Voc (V)	Jsc (mA/cm²)	FF (%)	PCE (%)
CdSe/BaHfS$_3$	0.7694	24.92921	48.15	9.23
Cu$_2$Te/BaHfS$_3$	0.8303	24.96952	70.52	14.03
BaSi$_2$/BaHfS$_3$	0.6555	26.89468	51.66	9.11
CuS/BaHfS$_3$	0.871	26.54864	72.01	16.65
Cu$_2$O/BaHfS$_3$	0.8536	26.00018	68.18	15.13
CuSCN/BaHfS$_3$	0.8581	25.59062	70.11	15.40
MoS$_2$/BaHfS$_3$	0.3523	22.96553	26.18	2.12
MoO$_3$/BaHfS$_3$	0.8426	25.6533	57.42	12.41

Table 5. Results obtained from the optimization of different Electron Transport Materials (ETM).

ETL MATERIALS	Voc (V)	Jsc (mA/cm²)	FF (%)	PCE (%)
BaHfS$_3$/Ti$_2$O$_3$	0.8608	29.85187	69.27	17.80
BaHfS$_3$/ZnO	1.7217	14.541913	39.95	10.00
BaHfS$_3$/WS$_2$	0.858	24.10394	70.98	14.68
BaHfS$_3$/Alq$_3$	0.8569	24.64323	72.62	13.77
BaHfS$_3$/ZnSnN$_2$	1.0069	8.113552	72.62	5.93
BaHfS$_3$/In$_2$S$_3$	0.8572	20.89708	76.51	13.71
BaHfS$_3$/C$_6$O	0.8893	25.51531	46.96	10.66
BaHfS$_3$/ZnMgO	0.8488	24.29653	49.51	10.21

4 Conclusion

$BaHfS_3$ is a lead-free absorber material notable for its optical absorption and stability. This research investigates BaHfS3-based solar cells through SCAPS-1D modeling, considering absorber thickness, bandgap, defect density, temperature, resistances, and transport materials. The base model (AZO/IGZO/$BaHfS_3$/Sb_2S_3) achieved 8.78 % efficiency, with 52.67 % fill factor, 19.90 mA/cm² short-circuit current density (Jsc), and 0.837V open-circuit voltage (Voc). Absorber thickness of 300-400 nm balances absorption and transport, with Voc decreasing to 0.84 V, Jsc increasing to 27 mA/cm², FF declining to 30 %, achieving 16.1 % efficiency. Bandgap tuning showed maximum η 16.2 % at 1.5 eV. Minimizing defect density to 1×10^{10} cm^{-3} improved performance to 19 % before decreasing to 3 % at 1×10^{18} cm^{-3}. Peak efficiency of 18.8 % occurred at 340-350 K. Under optimized conditions, efficiency reached 18.7 % with low Rs sensitivity (1–10 Ω·cm²). $MoSe_2$ buffer layer thickness of 1000 nm increased efficiency to 25.39 %. Ti_2O_3 proved the best ETM (η ≈ 17.80 %) and CuS the best HTM (η ≈ 16.65 %). The optimized TiO_2/$BaHfS_3$/CuS device achieved 19 % efficiency.

Acknowledgements

We are grateful to Prof. Marc Burgelman and his team at the University of Gent for providing us with access to the SCAPS-1D (Solar Cell Capacitance Simulator – 1 Dimension) software, which was essential for this study.

Declaration of Competing Interest

The authors declare that there is no conflict of interest.

References

[1] S. Pawar, Harnessing the Power of Renewable Energy: A Study of Sustainable Sources and Technologies, Journal of Research in Applied Science and Biotechnology 3 (2024) 163–169. https://doi.org/10.55544/jrasb.3.4.19.

[2] A. Balal, Y. Pakzad Jafarabadi, A. Demir, M. Igene, M. Giesselmann, S. Bayne, Forecasting Solar Power Generation Utilizing Machine Learning Models in Lubbock, Emerging Science Journal 7 (2023) 1052–1062. https://doi.org/10.28991/ESJ-2023-07-04-02.

[3] Md. T. Sarker, M. H. S. M. Haram, S. J. Shern, G. Ramasamy, F. Al Farid, Readiness of Malaysian PV System to Utilize Energy Storage System with Second-Life Electric Vehicle Batteries, Energies 17 (2024) 3953. https://doi.org/10.3390/en17163953.

[4] S. Kumar, K. Rathore, Renewable Energy for Sustainable Development Goal of Clean and Affordable Energy, International Journal of Materials Manufacturing and Sustainable Technologies 2 (2023) 1–15. https://doi.org/10.56896/IJMMST.2023.2.1.001.

[5] M. F. Rabbi, J. Popp, D. Máté, S. Kovács, Energy Security and Energy Transition to Achieve Carbon Neutrality, Energies 15 (2022) 8126. https://doi.org/10.3390/en15218126.

[6] M. K. Hossain et al., Photovoltaic Performance Investigation of $Cs_3Bi_2I_9$-Based Perovskite Solar Cells with Various Charge Transport Channels Using DFT and SCAPS-1D Frameworks, Energy & Fuels 37 (2023) 7380–7400. https://doi.org/10.1021/acs.energyfuels.3c00540.

[7] V. Kumar, S. Kumari, P. Kumar, M. Kar, L. Kumar, Structural Analysis by Rietveld Method and Its Correlation with Optical Properties of Nanocrystalline Zinc Oxide, Advanced Materials Letters 6 (2015) 139–147. https://doi.org/10.5185/amlett.2015.5632.

[8] A. Lafond, C. Guillot-Deudon, J. Vidal, M. Paris, C. La, S. Jobic, Substitution of Li for Cu in Cu_2ZnSnS_4: Toward Wide Band Gap Absorbers with Low Cation Disorder for Thin Film Solar Cells, Inorganic Chemistry 56 (2017) 2712–2721. https://doi.org/10.1021/acs.inorgchem.6b02865.

[9] M. Krause, S.-C. Yang, S. Moser, S. Nishiwaki, A. N. Tiwari, R. Carron, Silver-Alloyed Low-Bandgap $CuInSe_2$ Solar Cells for Tandem Applications, Solar RRL 7 (2023) 2201122. https://doi.org/10.1002/solr.202201122.

[10] D. Srinivasan, A.-D. Rasu Chettiar, L. Marasamy, Engineering $BaHfS_3$ with Zr Alloying to Improve Solar Cell Performance: Insights from SCAPS-1D Simulations, Materials Science and Engineering: B 315 (2025) 118126. https://doi.org/10.1016/j.mseb.2025.118126.

[11] B. K. Bareth, M. N. Tripathi, High Photovoltaic Performance of an Emerging Lead-Free Chalcogenide Perovskite $BaHfS_3$ under High Pressure, Solar Energy Materials and Solar Cells 282 (2025) 113445. https://doi.org/10.1016/j.solmat.2025.113445.

[12] N. El Hidaoui, F. Goumrhar, L. B. Drissi, O. Boudouch, R. A. Laamara, Evaluation of Chalcogenide Perovskites $BaHfS_3$ for Charge Transport in Energy Conversion Applications: Solar Cells, Photocatalytic Water Splitting and Thermoelectric, Computational Condensed Matter 46 (2026) e01202. https://doi.org/10.1016/j.cocom.2025.e01202.

[13] M. K. A. Mohammed, Optimizing Non-Toxic $(CH_3NH_3)_3Bi_2I_9$ Perovskite Solar Cells by SCAPS-1D, Physica Scripta 99 (2024) 125980. https://doi.org/10.1088/1402-4896/ad9221.

[14] E. M. Grumstrup, M. M. Gabriel, C. W. Pinion, J. K. Parker, J. F. Cahoon, J. M. Papanikolas, Reversible Strain-Induced Electron–Hole Recombination in Silicon Nanowires Observed with Femtosecond Pump–Probe Microscopy, Nano Letters 14 (2014) 6287–6292. https://doi.org/10.1021/nl5026166.

[15] X. Zheng, E. Colegrove, J. N. Duenow, J. Moseley, W. K. Metzger, Roles of Bandgrading, Lifetime, Band Alignment, and Carrier Concentration in High-Efficiency CdSeTe Solar Cells, Journal of Applied Physics 128 (2020) 053102. https://doi.org/10.1063/5.0013726.

[16] N. Shrivastav et al., Two-Terminal Tandem Solar Cell with Sb_2S_3/Sb_2Se_3 Absorber Pair: Achieving 14% Power Conversion Efficiency, Physica Scripta 98 (2023) 115110. https://doi.org/10.1088/1402-4896/ad000e.

[17] A. Hosen, S. R. A. Ahmed, Performance Analysis of SnS Solar Cell with a Hole Transport Layer Based on Experimentally Extracted Device Parameters, Journal of Alloys and Compounds 909 (2022) 164823. https://doi.org/10.1016/j.jallcom.2022.164823.

[18] T.A. Chowdhury, R.B. Arif, H. Israq, N. Sharmili, and R.S. Shuvo, SCAPS Numerical Design of $MoSe_2$ Solar Cell for Different Buffer Layers, Chalcogenide Letters 21 (2024) 175–187. https://doi.org/10.15251/CL.2024.212.175.

[19] K. Deepthi Jayan, V. Sebastian, Modelling and Comparative Performance Analysis of Tin-Based Mixed Halide Perovskite Solar Cells with IGZO and CuO as Charge Transport Layers, International Journal of Energy Research 45 (2021) 16618–16632. https://doi.org/10.1002/er.6909.

[20] T. A. Chowdhury, SCAPS Modeling and Performance Analysis of AZO/SnS_2/CZTS Solar Cells, Optics Continuum 3 (2024) 1341. https://doi.org/10.1364/OPTCON.527415.

[21] J. Guo et al., Effect of Selenium and Chlorine Co-Passivation in Polycrystalline CdSeTe Devices, Applied Physics Letters 115 (2019) 153901. https://doi.org/10.1063/1.5123169.

[22] M. N. Harif et al., Effect of Cu_2Te Back Surface Interfacial Layer on Cadmium Telluride Thin Film Solar Cell Performance from Numerical Analysis, Crystals 13 (2023) 848. https://doi.org/10.3390/cryst13050848.

[23] M. D. Hredoy Hossain, N. SURAYA, M. D. Eakub Ali, M. D. Momin Biswas, Analytical Analysis of High-Efficient Thin Film $BaSi_2/In_2S_3$ Solar Cell with SCAPS 1-D Simulation, EMERG – Energy Environment Efficiency Resources Global 11 (2025) 29–40. https://doi.org/10.37410//EMERG.2025.1.03.

[24] J. Chantana, T. Kato, H. Sugimoto, T. Minemoto, Investigation of Correlation Between Open-Circuit Voltage Deficit and Carrier Recombination Rates in $Cu(In,Ga)(S,Se)_2$-Based Thin-Film Solar Cells, Applied Physics Letters 112 (2018) 151601. https://doi.org/10.1063/1.5023828.

[25] C. Lin et al., The Investigation of the Influence of a Cu_2O Buffer Layer on Hole Transport Layers in $MAPbI_3$-Based Perovskite Solar Cells, Materials 15 (2022) 8142. https://doi.org/10.3390/ma15228142.

[26] S. Z. Haider, H. Anwar, M. Wang, Theoretical Device Engineering for High-Performance Perovskite Solar Cells Using CuSCN as Hole Transport Material to Boost the Efficiency Above 25%, Physica Status Solidi A 216 (2019) 1900102. https://doi.org/10.1002/pssa.201900102.

[27] S. Ghosh, S. Yasmin, J. Ferdous, B. B. Saha, Numerical Analysis of a CZTS Solar Cell with MoS_2 as a Buffer Layer and Graphene as a Transparent Conducting Oxide Layer for Enhanced Cell Performance, Micromachines 13 (2022) 1249. https://doi.org/10.3390/mi13081249.

[28] A. Zeinidenov, T. Mukametkali, B. Ilyassov, A. Aimukhanov, D. Valiev, The Effect of MoO_3 Interlayer on Electro-Physical Characteristics of the Perovskite Solar Cells, Synthetic Metals 281 (2021) 116903. https://doi.org/10.1016/j.synthmet.2021.116903.

[29] I. Jeong et al., Solution-Processed Ultrathin TiO_2 Compact Layer Hybridized with Mesoporous TiO_2 for High-Performance Perovskite Solar Cells, ACS Applied Materials & Interfaces 9 (2017) 36865–36874. https://doi.org/10.1021/acsami.7b11901.

[30] I. Qasim et al., Numerical Optimization of $(FTO/ZnO/CdS/CH_3NH_3SnI_3/GaAs/Au)$ Perovskite Solar Cell Using Solar Capacitance Simulator with Efficiency Above 23% Predicted, Optical and Quantum Electronics 53 (2021) 713. https://doi.org/10.1007/s11082-021-03361-5.

[31] Md. N. H. Riyad, A. Sunny, Most. M. Khatun, S. Rahman, S. R. A. Ahmed, Performance Evaluation of WS_2 as Buffer and Sb_2S_3 as Hole Transport Layer in CZTS Solar Cell by Numerical Simulation, Engineering Reports 5 (2023) e12600. https://doi.org/10.1002/eng2.12600.

[32] M. Méndez, E. Palomares, Alq_3 (tris(8-hydroxyquinolinato)aluminium) as a Selective n-Type Contact for FAMAPIBr Perovskite Solar Cells with Efficient Energy Transfer to Increase the Solar Cell Photocurrent, RSC Advances 7 (2017) 35525–35527. https://doi.org/10.1039/C7RA06645G.

[33] A. Laidouci, Mamta, V. N. Singh, P. K. Dakua, D. K. Panda, Performance Evaluation of $ZnSnN_2$ Solar Cells with Si Back Surface Field Using SCAPS-1D: A Theoretical Study, Heliyon 9 (2023) e20601. https://doi.org/10.1016/j.heliyon.2023.e20601.

[34] K. Deepthi Jayan, V. Sebastian, Comprehensive Device Modelling and Performance Analysis of $MASnI_3$-Based Perovskite Solar Cells with Diverse ETM, HTM and Back Metal Contacts, Solar Energy 217 (2021) 40–48. https://doi.org/10.1016/j.solener.2021.01.058.

[35] A. Srivastava, B. P. Pandey, Performance Analysis of CZTS Solar Cell with ZnS+ZnMgO as a Buffer Layer Using SCAPS-1D, Proceedings of the 2023 International Conference on Computer, Electronics & Electrical Engineering & Their Applications (IC2E3), IEEE, Srinagar Garhwal, India (2023) 1–6. https://doi.org/10.1109/IC2E357697.2023.10262440.

[36] Y. Chen et al., Multilayer Cascade Charge Transport Layer for High-Performance Inverted Mesoscopic All-Inorganic and Hybrid Wide-Bandgap Perovskite Solar Cells, Solar RRL 4 (2020) 2000344. https://doi.org/10.1002/solr.202000344.

[37] A. Crovetto et al., Interface Band Gap Narrowing Behind Open-Circuit Voltage Losses in Cu_2ZnSnS_4 Solar Cells, Applied Physics Letters 110 (2017) 083903. https://doi.org/10.1063/1.4976830.

[38] A. Fakharuddin et al., Robust Inorganic Hole Transport Materials for Organic and Perovskite Solar Cells: Insights into Materials Electronic Properties and Device Performance, Solar RRL 5 (2021) 2000555. https://doi.org/10.1002/solr.202000555.

[39] G. M. Mustafa, B. Younas, S. Saba, Z. M. Elqahtani, N. Alwadai, S. Aftab, Numerical Simulation to Optimize Power Conversion Efficiency of an $FTO/GO/Cs_2AgBiBr_6/Cu_2O$ Solar Cell, RSC Advances 14 (2024) 18957–18969. https://doi.org/10.1039/D4RA01559B.

[40] H. Bahador, Z. Abdoli, Enhancing Light Absorption in Ultra-Thin Perovskite Solar Cells Using Plasmonic Gold Nanoparticle Clusters, Physica Scripta 99 (2024) 105918. https://doi.org/10.1088/1402-4896/ad7074.

[41] P. Casper et al., Optoelectrical Improvement of Ultra-Thin $Cu(In,Ga)Se_2$ Solar Cells Through Microstructured MgF_2 and Al_2O_3 Back Contact Passivation Layer, Physica Status Solidi RRL – Rapid Research Letters 10 (2016) 376–380. https://doi.org/10.1002/pssr.201600018.

[42] I. Riedel, V. Dyakonov, Influence of Electronic Transport Properties of Polymer-Fullerene Blends on the Performance of Bulk Heterojunction Photovoltaic Devices, Physica Status Solidi A 201 (2004) 1332–1341. https://doi.org/10.1002/pssa.200404333.

[43] P. Ravirajan, S. A. Haque, J. R. Durrant, D. Poplavskyy, D. D. C. Bradley, J. Nelson, Hybrid Nanocrystalline TiO_2 Solar Cells with a Fluorene–Thiophene Copolymer as a Sensitizer and Hole Conductor, Journal of Applied Physics 95 (2004) 1473–1480. https://doi.org/10.1063/1.1638614.

[44] S. Maiti et al., Boosting the Efficiency of Quantum Dot-Sensitized Solar Cells Through Formation of the Cation-Exchanged Hole Transporting Layer, Langmuir 34 (2018) 50–57. https://doi.org/10.1021/acs.langmuir.7b02659.

[45] G. Xu et al., Integrating Ultrathin Bulk-Heterojunction Organic Semiconductor Intermediary for High-Performance Low-Bandgap Perovskite Solar Cells with Low Energy Loss, Advanced Functional Materials 28 (2018) 1804427. https://doi.org/10.1002/adfm.201804427.

[46] Y. Qin et al., Achieving 12.8% Efficiency by Simultaneously Improving Open-Circuit Voltage and Short-Circuit Current Density in Tandem Organic Solar Cells, Advanced Materials 29 (2017) 1606340. https://doi.org/10.1002/adma.201606340.

[47] W. Dou et al., Vacancy-Regulated Charge Carrier Dynamics and Suppressed Nonradiative Recombination in Two-Dimensional ReX_2 (X = S, Se), Journal of Physical Chemistry Letters 13 (2022) 10656–10665. https://doi.org/10.1021/acs.jpclett.2c02796.

[48] S. Pradhan, A. Stavrinadis, S. Gupta, G. Konstantatos, Reducing Interface Recombination through Mixed Nanocrystal Interlayers in PbS Quantum Dot Solar Cells, ACS Applied Materials & Interfaces 9 (2017) 27390–27395. https://doi.org/10.1021/acsami.7b08568.

[49] D. Chen et al., Solution-Processed, Inverted $AgBiS_2$ Nanocrystal Solar Cells, ACS Applied Materials & Interfaces 14 (2022) 1634–1642. https://doi.org/10.1021/acsami.1c17133.

[50] V. V. Brus et al., Temperature and Light Modulated Open-Circuit Voltage in Nonfullerene Organic Solar Cells with Different Effective Bandgaps, Advanced Energy Materials 11 (2021) 2003091. https://doi.org/10.1002/aenm.202003091.

[51] A. A. El-Naggar et al., Numerical Simulation Based Performance Enhancement Approach for an Inorganic $BaZrS_3/CuO$ Heterojunction Solar Cell, Scientific Reports 14 (2024) 7614. https://doi.org/10.1038/s41598-024-57636-4.

[52] S. Z. Oener et al., Metal–Insulator–Semiconductor Nanowire Network Solar Cells, Nano Letters 16 (2016) 3689–3695. https://doi.org/10.1021/acs.nanolett.6b00949.

[53] F. Wang et al., Full-Scale Chemical and Field-Effect Passivation: 21.52% Efficiency of Stable $MAPbI_3$ Solar Cells via Benzenamine Modification, Nano Research 14 (2021) 2783–2789. https://doi.org/10.1007/s12274-021-3286-2.

[54] X. Xiong, C. Ding, B. Jiang, G. Zeng, B. Li, An Optimization Path for $Sb_2(S,Se)_3$ Solar Cells to Achieve an Efficiency Exceeding 20%, Nanomaterials 14 (2024) 1433. https://doi.org/10.3390/nano14171433.

[55] Mamta, K. K. Maurya, V. N. Singh, Enhancing the Performance of an Sb_2Se_3-Based Solar Cell by Dual Buffer Layer, Sustainability 13 (2021) 12320. https://doi.org/10.3390/su132112320.

[56] G. Liang et al., Charge Separation Enhancement Enables Record Photocurrent Density in $Cu_2ZnSn(S,Se)_4$ Photocathodes for Efficient Solar Hydrogen Production, Advanced Energy Materials 13 (2023) 2300215. https://doi.org/10.1002/aenm.202300215.

[57] Z. Durmaz, S. Husein, R. Saive, Thin Silicon Interference Solar Cells for Targeted or Broadband Wavelength Absorption Enhancement, Optics Express 29 (2021) 4324. https://doi.org/10.1364/OE.413294.

[58] D. Grabowski, Z. Liu, G. Schöpe, U. Rau, T. Kirchartz, Fill Factor Losses and Deviations from the Superposition Principle in Lead Halide Perovskite Solar Cells, Solar RRL 6 (2022) 2200507. https://doi.org/10.1002/solr.202200507.

[59] N. K. Singh, A. Agarwal, Numerical Investigation of Electron/Hole Transport Layer for Enhancement of Ecofriendly Tin-Ge Based Perovskite Solar Cell, Energy Sources, Part A: Recovery, Utilization, and Environmental Effects 45 (2023) 3087–3106. https://doi.org/10.1080/15567036.2023.2192182.

[60] Z. Wang et al., Toward High Efficient $Cu_2ZnSn(S_x,Se_{1-x})_4$ Solar Cells: Breaking the Limitations of VOC and FF, Small 19 (2023) 2300634. https://doi.org/10.1002/smll.202300634.

[61] G. J. W. Aalbers, T. P. A. Van Der Pol, K. Datta, W. H. M. Remmerswaal, M. M. Wienk, R. A. J. Janssen, Effect of Sub-Bandgap Defects on Radiative and Non-Radiative Open-Circuit Voltage Losses in Perovskite Solar Cells, Nature Communications 15 (2024) 1276. https://doi.org/10.1038/s41467-024-45512-8.